Journal of Materials Chemistry A

Multi-walled carbon nanotube supported Manganese Selenide as Highly Active Bifunctional OER and ORR electrocatalyst

Journal:	*Journal of Materials Chemistry A*
Manuscript ID	TA-ART-11-2021-009864.R1
Article Type:	Paper
Date Submitted by the Author:	23-Jan-2022
Complete List of Authors:	Singh, Harish; Missouri University of Science & Technology, Chemistry Marley-Hines, McKenzie; Missouri University of Science & Technology, Chemical and Biochemical Engineering Chakravarty, Shatadru; Missouri University of Science & Technology, Advanced Materials Characterization Laboratory, Materials Research Center Nath, Manashi; Missouri University of Science & Technology, Chemistry

ARTICLE

Multi-walled carbon nanotube supported Manganese Selenide as Highly Active Bifunctional OER and ORR electrocatalyst

Received 00th January 20xx,
Accepted 00th January 20xx

DOI: 10.1039/x0xx00000x

Harish Singh[a], McKenzie Marley-Hines[a,b], Shatadru Chakravarty[c], Manashi Nath[a]*

Abstract

Transition metal selenides have attracted intensive interest as cost-effective electrocatalysts for oxygen reduction reaction (ORR) and oxygen evolution reaction (OER) because of the continuous thrust in sustainable energy conversion. In this article a Mn-based bifunctional electrocatalyst, MnSe has been identified which shows efficient OER and ORR activity in alkaline medium. The catalytic activity could be further enhanced by using multiwalled carbon nanotubes (MWCNT) which increases the charge transfer and electronic conductivity of the catalyst composite. This MnSe@MWCNT catalyst composite exhibits a very low overpotential of 290 mV at 10 mA cm^{-2}, which outperforms state-of-the-art RuO_2 as well as other oxide based electrocatalysts. Furthermore, the composite's facile OER kinetics was evidenced by its small Tafel slope of 54.76 mV dec^{-1} and low charge transfer resistance, indicating quick transport of the reactant species. The MnSe@MWCNT also exhibited efficient electrocatalytic activity for ORR with a E_{onset} of 0.94 V, which is among the best reported till date for chalcogenide based ORR electrocatalysts. More importantly, this MnSe-based ORR electrocatalyst exhibits high degree of methanol tolerance, showing no degeradation of catalyst performance in presence of copious quantities of methanol, thereby out-performing state-of-the-art Pt electrocatalyst. The catalyst compositie also exhibited exceptional functional and compositional stability for OER and ORR after prolonged period of continuous operation in alkaline medium. The surface Raman analysis after OER revealed the retention of manganese selenide surface with evidence of oxo coordination confirming the formation of (oxy)selenide as the active surface for OER. Such efficient bifunctional OER and ORR activity makes this MnSe based catalyst attractive for overall electrolysis in regenerative as well as direct methanol fuel cells.

Keywords: Oxygen reduction reaction, Oxygen evolution reaction, bifunctional catalysts, Methanol Tolerance

Introduction

The perils of global warming and environmental pollution will be critical in the near future, forcing researchers to find a potential solution for clean energy generation from sustainable resources. Among the various solutions being pursued, regenerative fuel cells have attracted considerable attention due to escalating energy demands, and environmental concerns. Renewable energy technologies such as regenerative fuel cells (RFC), electrocatalytic water splitting (EWS), and metal-air batteries (MAB) include the fundamental electrochemical reactions from oxygen reduction (ORR) to oxygen evolution (OER). These alternative "clean" energy technologies are supported through the use of electrocatalysts that increase efficiency of these fundamental energy conversion processes. Precious metal-based materials, such as Pt and RuO_2, are widely regarded as state-of-the-art electrocatalysts for ORR and OER, respectively.[1–4] However, their large-scale application is limited by the economic constrains and insufficient reserves for the precious elements Pt and Ru. Intensive research over the last few years on the other hand, have resulted in identification of several non-precious metal-based systems as highly efficient OER and ORR electrocatalysts. In particular, transition metal oxides,[5] chalcogenides,[6–9]pnictides,[9,10] and layered double hydroxides (LDHs) have shown promising OER electrocatalytic activity. On the other hand, heteroatom-doped carbon materials, Fe, Co, and Mn-based metal hydroxide, and chalcogenides have shown promise as potential electrode materials for ORR in fuel cells.[6,11–15]

The oxygen evolution reaction (OER) and the oxygen reduction reaction (ORR) take place at the same electrode in electrochemical devices (EWS, MAB, or RFC), making it a bifunctional electrode, wherein OER can be considered as charging while ORR is the discharging process. However, due to a scarcity of bifunctional oxygen electrodes which can support

[a] Department of Chemistry, Missouri University of Science and Technology, Rolla, MO 65409, USA.
[b] Department of Chemical and Biochemical Engineering, Missouri University of Science and Technology, Rolla, MO 65409, USA.
[c] Advanced Materials Characterization Laboratory/Materials Research Center, Missouri University of Science and Technology, Rolla, Missouri 65409, United States.
† Electronic Supplementary Information (ESI) available: Supporting information includes ECSA, chronoamperometry study, Raman Spectra, XRD, SEM, XPS after chronoamperometry studies, LSV before and after chronoamperometry studies of Pt/GCE.

both OER and ORR, that would also require the electrocatalysts to be electrochemically stable over a wide range of potentials, these renewable energy technologies are still facing limitations for practical usage. Several bifunctional electrocatalysts have recently been investigated, including alloys of Pt and Ir/Ru catalysts, for ORR and OER.[16–18] However, the high cost of precious metals, precludes their widespread use in electrochemical energy conversion and storage devices. As far as general electrochemical activities are concerned, they also have intrinsic disadvantages, such as high activation barrier, low specific capacitance, unstable chemical structures, and limited cycle lives. To overcome these concerns, research has focused on non-precious transition metal based compositions wherein several bifunctional catalysts have been developed for both ORR and OER that include Co_3O_4/CNTs,[19] Mn_xO_y/NC,[20] Co_xO_y/NC,[20] $Ni_xCo_yO_4$/Co–NG,[21] and $BaTiO_{3-x}$.[22]

Recently, catalysts based on transition metal chalcogenides (TMCs) have gained considerable attention compared to metal oxides and alloys because of their unprecedented high activity.[23–26] This is especially relevant because the rich stoichiometry alterations possible in metal-rich chalcogenides make them highly efficient, inexpensive, and robust as well as a viable substitute for noble metals as electrocatalysts for OER and ORR. TMCs also have promising prospects for use in sensors[27,28] as well as in a plethora of emerging renewable energy technologies.[29–33] Among nonprecious metal-based catalysts, Ni and Co-based compositions have been studied widely for electrocatalytic activities.[8,21,30,34] One of the critical criteria necessary for improved electrochemical activity is that the catalytic centre should exhibit facile electrochemical tuning with low energy barrier. This can be achieved by using transition metals that can shuttle between various stable oxidation states. In that regards, Mn-based compositions can be very attractive since Mn can achieve various oxidation states with ease. Moreover, such Mn-based compounds are also lucrative due to their rich electrochemical properties, high abundance, low cost, and less toxicity. However, there has been few reports of Mn-based compounds that has been used as OER catalysts,[25,26] and as ORR catalysts (mainly oxides) in alkaline batteries.[35,36] It has been observed that the valence state of Mn is critical for ORR performance, as the Mn(III) ion in MnO_x typically exhibits greater activity than the Mn(II) or Mn (IV). In our current investigation, an attempt has been made to modify the oxidation state of Mn by synthesizing MnSe which further helped to develop a bifunctional OER/ORR catalyst.

A major drawback of the TMCs in terms of their limited conductivity have hindered their use for largescale industrial application in oxygen electrocatalysis.[37,38] Carbon materials, on the other hand, due to their high electrical conductivity and specific surface area, provide reliable and consistent support for the integration and assembly of electrocatalysts.[39,40] Earth-abundant conductive carbon materials and their derivatives, such as carbon nanotubes (CNTs) and graphene along with non-precious metal based electrocatalysts thus have the capability to replace noble metal alloys in practical fuel cell applications.[41] Multi-walled carbon nanotubes (MWCNTs) have unique thermal and mechanical properties that make them appealing for the development of new materials, in addition to the electrical properties that they inherit from graphene.[42,43] Their hollow interiors can be filled with a variety of nanomaterials, isolating and shielding them from their surrounding environment - an extremely useful property for fuel cell application.[44–46] The numerous surface defects on the carbon support results in abundant homogeneous nucleation sites, and in conjunction with strong coordination interactions, this provides numerous sites for nanoparticle stabilization, resulting in increased specific surface area that leads to enhanced catalytic activity. Furthermore, their enhanced electron transfer and mass diffusion properties can also be used to improve OER and ORR current density.[47–49] Recently, Lee and co-workers have also reported a series of studies on WS_2–CNTs composites which demonstrates surprisingly better performance in OER and ORR compared to support-free WS_2.[50] Nevertheless, carbon material by themselves are not sufficiently active and stable as a bifunctional catalyst, especially when it is prone to serious corrosion under a high anodic potential as well as in a highly alkaline medium.[51,52] The absence of carbon, on the other hand, would result in a low conductivity of the catalyst, reducing the efficiency of electrocatalysis. However, the controlled synthesis of nano-heterostructures integrating multiple nanostructures is challenging and usually uses more complex and expensive multi-step synthesis processes.[53,54]

In the present study, MnSe nanostructures have been investigated as bifunctional electrocatalyst for OER and ORR in alkaline medium. The MnSe nanostructures were also mixed with carbon nanostructures to form hybrid composites to see if they can compensate for each other's shortcomings to ameliorate the catalytic activities. Herein, we provide a protocol for the development of a MnSe@MWCNT bifunctional catalyst that can simultaneously perform OER and ORR reactions with high efficiency, superior stability and also exhibits methanol tolerance in an alkaline solution. In this study, the MnSe@MWCNT hetero-nanostructures were produced by a facile one-pot synthesis strategy using an in-situ solvothermal reaction of MWCNT with manganese and selenium sources. The MnSe@MWCNT composite was synthesized through one-step hydrothermal synthesis process at a moderately low temperature. The MnSe@MWCNT composite showed an overpotential of 290 mV at 10 mA/cm^2 which is significantly better than state-of-the-art precious metal oxides and comparable to some of the best OER electrocatalysts reported so far.[55,56] Although manganese selenide based compositions has been recently reported as OER electrocatalysts,[25,26] it must be noted that in these previous reports, the MnSe composition was doped with other transition metals such as Fe, Co etc. Such doping has been known to alter composition of the catalytically active site, changing its intrinsic activity. Moreover, pure MnSe and MnSe@MWCNT composite reported in this article shows comparable activity with previously reported MnSe-based doped systems,[25] even when grown on 2-dimensional OER-inactive substrates as opposed to Ni foam which leads to significantly enhanced activity due to substrate effect. To the best of our knowledge, this is the first report of pure manganese selenide (MnSe) as bifunctional OER/ORR electrocatalyst with

high efficiency and high methanol tolerance. This current study not only paves the way for the development of new nonprecious metal-based ORR/OER electrocatalysts with superior stability while maintaining high activities, but it also paves the way for carbon-metal chalcogenide composites to be used as novel electrocatalysts in more energy conversion and storage processes. In addition to exhibiting excellent bifunctional OER/ORR activity this catalyst composition also exhibits superior methanol tolerance and stability over platinum@glassy carbon (Pt/GCE) electrode. In this manuscript we have reported not only a bifunctional catalyst but have provided new knowledge about evolution of the active surface composition and how to increase efficiency and functionality of the catalyst composite.

Experimental

Materials

All the reagents were of analytical grade and were used as received. Manganese chloride ($MnCl_2.4H_2O$) was obtained from Fisher Scientific. Sodium selenite (Na_2SeO_3) and hydrazine hydrate ($N_2H_4{\cdot}H_2O$) were purchased from Alfa Aesar and Acros Organics respectively. MWCNTs (~1-5 μm in length, 20–25 nm in outer diameter) were purchased from Strem chemicals INC. and treated in 3 M HNO_3 solution at 80°C for an hour before being used. Before usage, the Ni foam was soaked in dilute hydrochloric acid for 10 minutes and then cleaned several times with acetone, ethanol, and distilled water.

Synthesis of MnSe: For the synthesis of manganese selenide, firstly, 0.2 M Na_2SeO_3 and 0.1 M $MnCl_2{\cdot}4H_2O$ were dissolved into 8 mL deionized water. After mixing for 20 min under vigorous stirring, $N_2H_4{\cdot}H_2O$ (2 ml) was added to the mixture, and the mixture was stirred continuously for another 20 minutes. The final mixture was sealed in a 23 ml Teflon-lined stainless-steel autoclave and heated at 145 °C for 24 h. For direct growth of MnSe on Nickel foam (MnSe/NF), pre-cleaned Ni foam was placed inside the Teflon-liner. The autoclave was then allowed to cool down naturally. The final black colored product was then centrifuged and washed several times with a mixture of ethanol and deionized water. Finally, the product obtained was dried at 60°C in a vacuum oven. When Ni foam was used for direct growth, the as obtained MnSe/NF was also rinsed several times with DI water and ethanol, and then dried at 60 °C in vacuum oven.

Synthesis of MnSe@MWCNT Composite:

The MnSe@MWCNT composite was prepared as follows: 0.2 M Na_2SeO_3 and 0.1 M $MnCl_2{\cdot}4H_2O$ were dissolved into 8 mL deionized water and added to a 23 mL Teflon-lined stainless autoclave. Then 2 mL of $N_2H_4{\cdot}H_2O$ was added with vigorous stirring for 20 min. Finally, MWCNTs (2 mg) were added rapidly to the reaction mixture and stirred until being completely dissolved. For direct growth of MnSe@MWCNT on Nickel foam (MnSe@MWCNT/NF), pre-cleaned Ni foam was also placed inside the Teflon-liner. The autoclave was sealed and maintained at 145 °C for 24 h. After cooling to room temperature naturally, the products were centrifuged, washed several times with a mixture of ethanol and deionized water, and dried under vacuum at 60°C overnight. Similarly, when Ni foam was used, the as obtained MnSe@MWCNT/NF was rinsed several times with DI water and ethanol, and then dried at 60 °C in vacuum oven.

Electrode preparation

To analyse the OER and ORR activity of hydrothermally synthesized MnSe and MnSe@MWCNT catalysts, a homogeneous catalyst ink was prepared by dispersing 4 mg of catalyst in 300 μL of ethanol mixed with Nafion (0.8 μL 5 wt. %). For OER studies, this mixture was ultra-sonicated for about 1 h to prepare a homogeneous ink. 100 μL of the ink was drop casted onto carbon cloth (geometric area of 0.283cm^{-2}). Before ORR studies, the glassy carbon electrode (GC) was polished with 1 and 0.05 μm alumina powder as well sonicated first in isopropanol and distilled water. The catalyst ink (20 μL) was then drop casted on the glassy carbon working electrode (geometric area of 0.196 cm^{-2}) and dried under ambient condition.

Materials Characterization

The crystallinity of the as-synthesized samples was analysed by powder X-ray diffraction (PXRD) using Philips X-Pert X-ray diffractometer (PANalytical, Almelo, The Netherlands) with CuKα source (1.5418 Å) radiation). The morphology of the samples was examined by scanning electron microscope (SEM, Hitachi S4700) using an accelerating voltage of 15 kV and a working distance of 10 mm. The as-synthesized samples were dispersed directly on the formvar-coated Cu TEM grid and analysed with Tecnai F20 to collect high-resolution TEM images (HRTEM). The chemical composition of catalysts and the valence states of the elements were determined by X-ray photoelectron spectroscopy (XPS). The chemical composition was also analysed before and after the OER and ORR stability studies. All XPS analyses were conducted without sputtering on the pristine catalyst surface. The Raman spectra of all synthesized samples were collected with LabRam ARAMIS (HORIBA Jobin-Yvon Raman spectrometer equipped with a CCD detector). A Thermo Scientific NEXSA surface analysis equipment was used to perform simultaneous XPS and surface Raman analyses. By combining both methodologies on the same platform, it is possible to examine the same positions concurrently on surface to gain complete understanding of the material under optimal conditions in ultrahigh vacuum. The Nexsa system was equipped with a Thermo ScientificiXR Raman system (spectral dispersion of 2 cm^{-1} per CCD pixel element), with the Raman laser probe aligned with the X-ray spot. The surface Raman spectra were collected using 532 nm laser with 2 mW output power and a 16 s acquisition duration. Calibration was performed using the 520 cm^{-1} Raman peak of a silicon reference standard. The Raman system features four aperture settings (25 μm and 50 μm pinholes, and 25 μm and 50 m slits) that may be changed based on different sample features. The Raman spectrum signal was maximized by using a 50 μm slit.

Electrochemical Characterization

The OER and ORR electrocatalytic performances of as-prepared electrodes were studied by using an IviumStat potentiostat. The electrochemical measurements were performed in a three-electrode cell system with a graphite rod as the counter electrode, and Ag|AgCl (KCl-saturated) as the reference electrode. The 5 mm diameter rotating ring disk electrode (RRDE) was used as a working electrode for ORR while catalyst loaded carbon cloth was used for OER studies. For OER studies N_2-saturated 1 M KOH was used and for ORR studies, RRDE test was carried out in an O_2-saturated 1 M KOH at different rotation rates between 400 and 2000 rpm (10 mV s^{-1}).

The Koutecky-Levich (K-L) plots (J–1 vs. $\omega^{-1/2}$) were obtained at different potentials between 0.2 V to 0.8 V and fitted in linear curves by using the following K-L equation, to calculate the number of electrons transferred (n):[57]

$$1/J = 1/J_L + 1/J_K = 1/B\omega^{1/2} + 1/J_K \quad \text{Eq-1}$$

where J is the obtained current density (mA cm^{-2}), J_K and J_L are the kinetic and diffusion-limiting current densities respectively, and ω is the rotating rate (rpm). B is determined from the slope of K-L plots based on the Eq. (2):

$$B = 0.62nFC_0 (D_0)^{2/3}\upsilon^{-1/6} \quad \text{Eq-2}$$

Here, F is the Faraday constant (96485 C mol^{-1}), n is the number of electrons transferred per molecule of oxygen, C_0 is the bulk concentration of O_2 ($1.2 \times 10{-}6$ mol cm^{-3}), D_0 is the coefficient of diffusion of O_2 ($1.9 \times 10{-}5$ cm^2 s^{-1}), and v is the kinematic viscosity of the electrolyte (0.01 cm^2 s^{-1}).

Tafel plot: A key measurement to examine OER activity is the Tafel slope, which is calculated using the Tafel equation by fitting polarization data. As illustrated in Eq-3, the Tafel equation is the dependency of overpotential η on current density j.

$$\eta = a + 2.3RT/\alpha nF \log j \quad \text{Eq-3}$$

where α is the transfer coefficient, n is the number of electrons involved in the reaction, and F is the Faraday constant.

Electrochemically Active Surface Area (ECSA): Surface area of the catalyst has a significant impact on its catalytic activity. Thus, the electrochemically active surface area (ECSA) was determined using double-layer capacitance (C_{DL}) in accordance with eq. 4:

$$ECSA = C_{DL}/ C_S \quad \text{Eq-4}$$

Where C_{DL} is the double layer capacitance and C_S is the specific capacitance. Similar to previously reported metal selenide-based catalysts, Cs = 0.04 mF cm^{-2} was employed to estimate ECSA.[58,59] The C_{DL} was calculated by averaging the absolute values of cathodic and anodic slopes. In a non-stirred N_2 saturated 1.0 M KOH solution, the double layer current (i_{DL}) was measured using cyclic voltammograms (CVs) at different scan rates.

$$i_{DL} = C_{DL} \times v \quad \text{Eq-5}$$

Another important parameter is the Roughness Factor (RF) which defines surface roughness of the catalyst composite and can affect the observed catalytic properties. Ratio of ECSA to geometric electrode area (0.283 cm^2) was used to calculate RF.

Result and Discussion

The as-synthesized catalysts were characterized using various techniques to determine their structural and morphological composition. PXRD was utilized to confirm the structural and phase purity of hydrothermally synthesized samples. Figure 1a shows the comparison of PXRD patterns of MnSe, MnSe@MWCNT, and MWCNT. The PXRD data confirmed formation of pure MnSe corresponding to a cubic structure (lattice parameters a = b = c = 5.462Å) in Fm3m space group (225) [JCPDS No. 00-011-0683]. The presence of sharp diffraction peaks indicates the sample's purity and crystallinity. The as-synthesized MnSe@MWCNT hybrid material showed a similar PXRD pattern to that of the cubic MnSe phase indicating that formation of composite with MWCNT did not affect crystallinity or phase purity of MnSe. MWCNT on the other hand, did not show any diffraction peaks in the MnSe@MWCNT composite, perhaps due to the small carbon content and the relatively low diffraction intensity of the MWCNT peaks. Nevertheless, the presence of carbon nanotubes in the

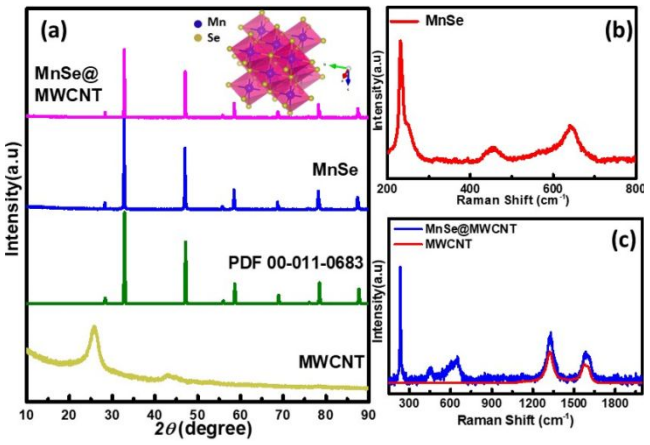

Figure 1. PXRD patterns of (a) MnSe@MWCNT, MnSe, and MWCNT compared with MnSe standard pattern. Raman spectra of as-synthesized (b) MnSe and (c) MnSe@MWCNT (blue curve) compared with that of MWCNT (red curve).

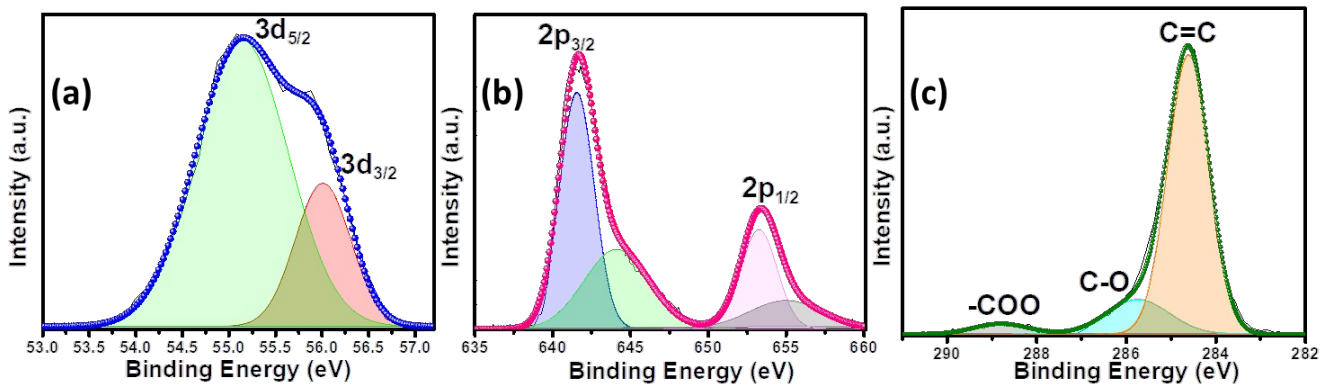

Figure 2. The deconvoluted XPS spectra of MnSe@MWCNT composite electrode showing (a) Se 3d (b) Mn 2p (C) C 1s peaks.

MnSe@MWCNT composite material was confirmed by Raman spectroscopy, XPS, and as well as from TEM.

Raman spectra of the MnSe sample was measured in the 200-800 cm^{-1} spectral range. Additionally, the peaks of Se–Se stretching mode are observed at 254.44, 456.58 cm^{-1}, and 646.28 cm^{-1} as shown in Figure 1b, being close to the values previously reported.[60,61] The Raman spectrum of MnSe@MWCNT and pristine MWCNT showed the characteristic D band (1342 cm^{-1}) and G band (1572 cm^{-1}) as shown in Figure 1c, which results from disorder and sp^2 hybridized carbon atoms in MWCNT walls. The I_D/I_G ratio of the MnSe@MWCNT sample was found to be 1.42, which represents a large number of defects on the carbon nanotube surface.[62] To investigate the surface elemental configuration and electronic states of the MnSe, X-ray photoelectron spectroscopy (XPS) was performed. Figure 2 shows the XPS spectra where the peaks can be attributed to Mn 2p3/2, Mn 2p1/2, Se 3d5/2, and Se 3d3/2. From the deconvoluted spectrum of Mn, the peaks at 642.61 and 654.27 suggest the existence of Mn^{2+} and Mn^{3+}. The presence of such mixed oxidation states in MnSe is consistent with the previously reported values.[63] The Se 3d peak at 55.2 eV and the smaller peak at 56.0 eV are ascribed to Se 3d5/2, and Se 3d3/2 respectively . Interestingly, there was no evidence of Mn-oxide phase confirming that these samples were primarily of selenide composition. The C 1s spectra from the MnSe@MWCNT sample on the other hand, showed peaks corresponding to C=C and carboxylate functionality arising from graphitic surface and functionalization of the MWCNT, respectively.

SEM and TEM analysis were performed to investigate the morphology of MnSe and MnSe@MWCNT composites. The MnSe sample showed uniform dense structures with sizes in the range of 3-5 µm, as shown in the SEM image in Figure 3a. The MnSe@MWCNT composites after hydrothermal reaction on the other hand, showed MWCNT backbones decorated with numerous MnSe cubes or spheres as shown in Figure 3b, where the light gray tubular-like agglomeration are the MWCNTs, while the cube-like particle is MnSe. A closer examination of the particle surface of both samples reveals that they have a multitude of small nanoparticles in range of 30-60 nm range. TEM images of MnSe (Figure 3 c) and MnSe@MWCNT (Figure 3 d) reveals the nanometer size particles distribution. In addition, Figure 3e and 3f shows the high-magnification TEM images showing lattice fringes with a clear interplanar spacing of 0.27 nm corresponding to (200) lattice planes of MnSe confirming crystallinity of these nanostructured grains.

Electrocatalytic Performance for OER

The electrocatalytic studies were performed using a standard 3-electrode set-up with glassy carbon (GC), Ag|AgCl, and MnSe/MnSe@MWCNT on carbon cloth as counter, reference, and working electrode, respectively. The hydrothermally

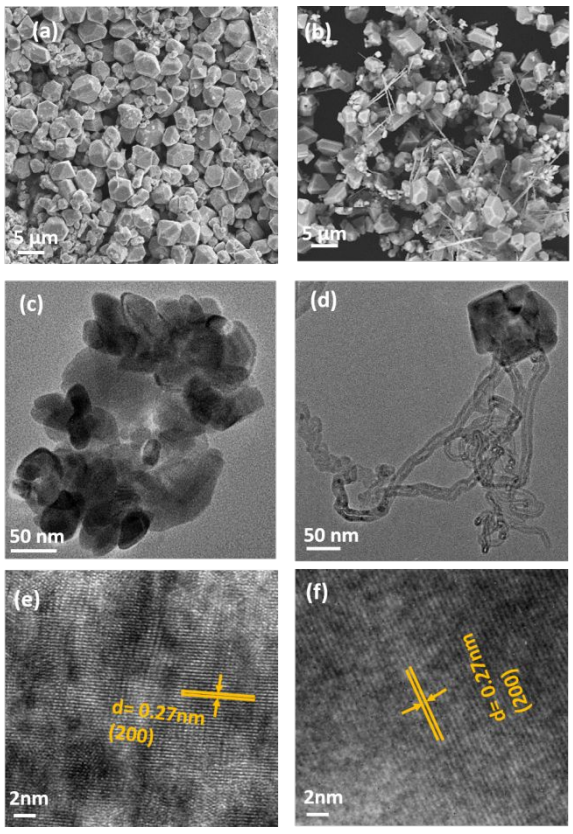

Figure 3. SEM images of (a) MnSe and (b) MnSe@MWCNT composite. TEM images of (c) MnSe and (d) MnSe@MWCNT composite. HRTEM images of (e) MnSe and (f) MnSe@MWCNT composite showing the fringes corresponding to (200) lattice planes of MnSe.

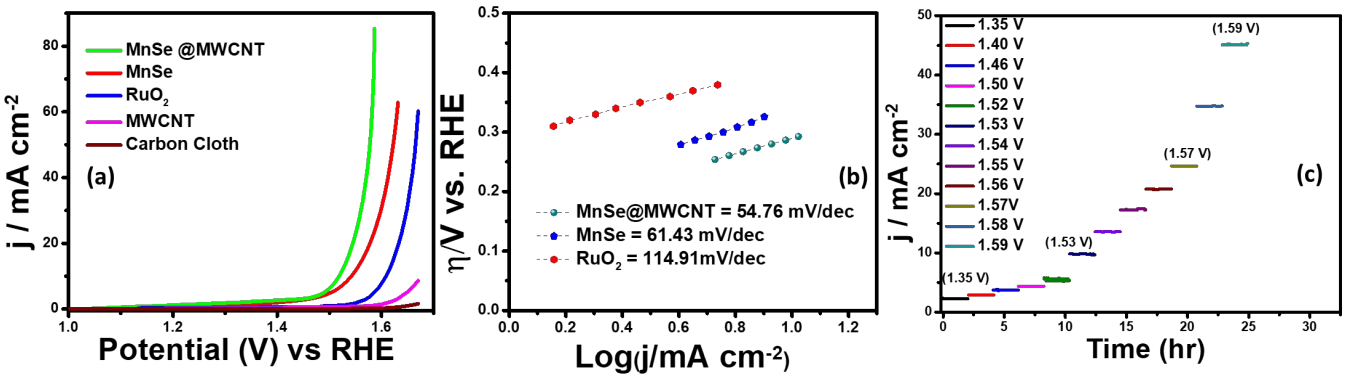

Figure 4. LSV plots of the as-prepared MnSe, MnSe@MWCNT, MWCNT on carbon cloth electrode compared with RuO_2 in 1 M KOH solution measured with a scan rate of 10 mV s^{-1}, confirming enhanced OER activity of MnSe and MnSe@MWCNT modified electrodes. (b) The Tafel plots MnSe, MnSe@MWCNT and RuO_2. (c) Multistep chronoamperometry (MCA) test of MnSe@MWCNT composite electrode were carried out at various constant applied potentials.

synthesized samples were drop-casted on carbon cloth as per methodology described above to prepare the working electrodes. The electrochemical studies for OER were performed using linear sweep voltammetry (LSV) as well as one-step and multistep constant potential chronoamperometric techniques. The OER activity of as-synthesized samples was determined using LSV at a scan rate of 10 mV s^{-1}. The resistance of 1.0 M KOH was estimated to be 15.0 Ω and was used for iR correction of all the LSV plots reported in this work. The OER activity of MnSe and MnSe@MWCNT was compared with state-of-the-art catalyst RuO_2 which was prepared using electrodeposition following a typical procedure outlined in the supporting information. Figure 4a shows the OER activity of MnSe, MnSe@MWCNT, and RuO_2 in N_2-saturated 1.0 M KOH. The OER onset potentials of MnSe, MnSe@MWCNT and RuO_2 were estimated to be 1.49,1.47, and 1.57 V, respectively. The overpotential at 10 $mAcm^{-2}$ (η_{10}) for MnSe, MnSe@MWCNT, and RuO_2 were estimated to be 310, 290, and 380 mV, respectively. The LSV plots also showed that both MnSe and MnSe@MWCNT had better OER catalytic activity compared to RuO_2. Interestingly, it was observed that the overpotential of MnSe@MWCNT composite dropped significantly compared to MnSe signifying the positive effect of mixing with MWCNT. Apart from low overpotential, the MnSe@MWCNT composite also showed higher current density indicating that the highly conducting MWCNT facilitated charge transfer within the catalyst composite. The overpotential of MnSe@MWCNT is comparable with some of the best OER electrocatalysts reported till date. As shown in Table S1, (Supporting Information).

Another important criterion for evaluating an electrocatalyst's OER performance is steady-state activity and durability under conditions of continuous operation. As shown in Figure 4c, multistep chronoamperometry measurements for OER were performed at various constant applied potentials to evaluate the electrochemical stability for MnSe@MWCNT electrode. Specifically, in this experiment, the potential steps were varied from 1.35 V to 1.59 V vs RHE where current density at each step was measured for ~2 h as shown in Figure 4c. It was observed that during long-term testing, there was no obvious deterioration of current density under different applied potentials, further confirming the excellent stability at low and high current density, prominent mass transport, and mechanical robustness toward OER activity. To compare the OER activity of MnSe and MnSe@MWCNT composite with other reported transition chalcogenides grown on metallic foam electrodes, and understand the effect of substrate, the MnSe and MnSe@MWCNT catalyst composite were also assembled on Ni foam either through direct hydrothermal synthesis or drop-casting as described in the methods section. It was observed that the catalyst composite showed significantly enhanced current density at lower overpotential (210 mV at 50

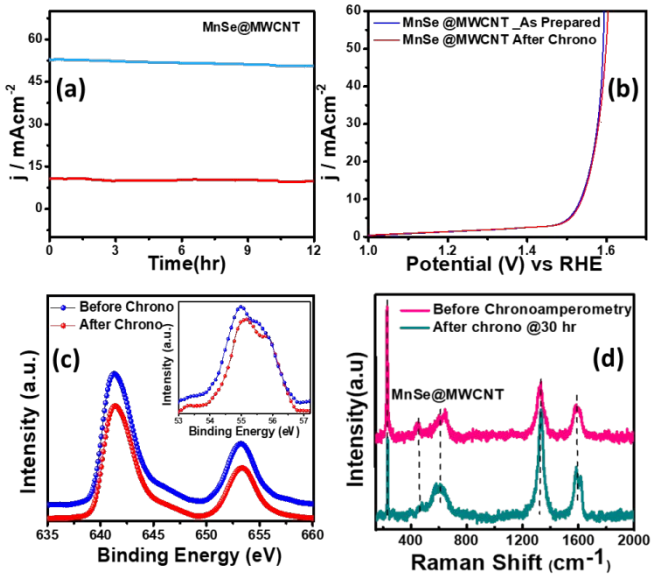

Figure 5. (a). Chronoamperometry plots illustrating long-term stability of MnSe@MWCNT modified electrode under constant overpotentials required to maintain current density at 10 and 50 mA cm^{-2}. (b) Comparison of LSV plots for MnSe@MWCNT before and after of chronoamperometry. (c) Comparison of the XPS peaks of Mn 2p and Se 3d (inset) before and after OER activity demonstrating catalyst's robustness. (d) Raman spectra of MnSe@MWCNT before and after OER chronoamperometry.

mA/cm^2) when grown on Ni foam (Figure S1(a)), wherein the overpotentials were estimated from reverse sweep of the CV plots as shown in Fig. S1(b). The higher current density on Ni foam can be attributed to the 3-dimensional porous mesh-like architecture for Ni foam and its inherent OER activity. The overpotentials at higher current densities between MnSe-based composites and other reported systems are also compared in Table S2. The ultimate usability of water electrolyzers can also be estimated by its ability to produce higher current density with less energy expense (i.e. lower overpotential). If a catalyst can produce higher current density, it signifies better potential for usage in practical devices. However, since we are interested in understanding the true intrinsic catalytic activity of these MnSe composites, further studies were conducted with carbon cloth as the substrate, which did not show any inherent activity. Tafel slope and turnover frequency are critical parameters for determining the intrinsic catalytic activity of as-synthesized nanostructures and for comprehending the OER mechanism. The Tafel plot is considered to be one of several methods for correlating the kinetic and thermodynamic properties of electrocatalytic systems and determining the rate at which oxidation current increases in response to the applied potential. The smaller the value of the Tafel slope, faster is the reaction kinetics, which can increase current density and thus oxygen generation. In Figure 4b, the Tafel slope values demonstrate that MnSe@MWCNT has the lowest Tafel slope of 54.76 mV dec^{-1} which even outperforms the RuO_2 catalyst (114.91 mV dec^{-1}). The low Tafel slope of MnSe@MWCNT suggests that it has comparable or better OER activity than most other recently reported Mn-based selenide OER catalysts (Table S1). Another important factor for OER catalytic activity is the electrochemically active surface area (ECSA). An increase in ECSA typically results in enhanced exposure of the active sites which boosts catalytic performance.[58,64] For direct comparison, the ECSA of each electrode was compared by estimating double layer capacitance in non-Faradaic region obtained from cyclic voltammetry (CV) plots as shown in Figure S2, (supporting information). The CV plot of each catalyst and corresponding capacitive current at 0.1 V versus Ag/AgCl were recorded at different scan rates in 1 M KOH to determine the ECSA which were estimated to be 10.48 and 19.3 cm^2 for MnSe and MnSe@MWCNT, respectively. Increased ECSA results in increased surface roughness factor (RF), which can be considered as another factor that influences catalytic activity which is typically enhanced by rough catalytic surface since more catalytic sites are exposed to the electrolyte. The RF value obtained for the MnSe@MWCNT electrode (68.2) is almost two times the value for the MnSe electrode (37.03), which is in good agreement with the improved catalytic activity observed for MnSe@MWCNT nanocomposite. Table 1 represents the comparison of electrocatalytic parameters of all the catalysts for OER activity reported in this article.

The long-term functional stability for the catalysts were also studied by chronoamperometry where a constant potential was applied, and the current density was measured for extended period. Figure S3, shows the 12 h stability studies for MnSe and MnSe@MWCNT modified electrodes at an applied potential of

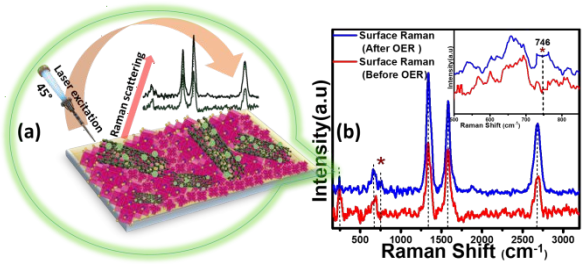

Figure 6. (a) Schematic representation for measuring surface Raman spectra. (b) Surface Raman spectra of MnSe@MWCNT composite before and after OER chronoamperometry for 12 h. Inset shows magnified spectra from 500 to 850 cm^{-1}.

1.55 and 1.52 V, respectively to achieve 10 mA cm^{-2} current density. It was observed that both electrodes showed extensive stability for 12 h with minimal degradation of current density (9.8% and 4.7% for MnSe and MnSe@MWCNT, respectively). It must be noted here that most cutting-edge OER electrocatalyst are maintained as carbon-free owing to the degradation of carbon under high anodic potential required for OER. However, in this case, the presence of MWCNT in the MnSe@MWCNT composite doesn't show any instability in catalytic performance or durability under long term operation. The long-term stability of the composite MnSe@MWCNT electrode was also measured at 10 and 50 mA cm^{-2} current density as shown in Figure 5a, which illustrated extensive stability of these catalysts even at higher current density. As shown in Figure 5b, there was no change in LSV even after long-term multistep chronoamperometry for 12 hours in the MnSe@MWCNT sample. These studies, specifically, multistep, and long-term chronoamperometry results not only confirm extended functional stability of these OER catalysts, but also demonstrates the positive effect of carbon support on improving surface stability of metal chalcogenide electrocatalysts which leads to more efficient OER activity. This also validated the superior mass transport property and suggesting its superior operational stability in alkaline media.

The compositional stability of these electrocatalysts after extended period OER studies was investigated with PXRD, XPS and Raman spectroscopy. Typically, PXRD, XPS, SEM and Raman were collected from the catalyst composite after 12 h chronoamperometry study in 1 M KOH electrolyte. The XPS data of MnSe@MWCNT composite revealed that there was no change of oxidation states and XPS peak positions of either Mn or Se as shown in Figure 5c, confirming compositional stability of the catalyst composite. Further information about the catalyst compositions before and after OER was provided by Raman spectra. Interestingly, it was observed that the Raman spectra of the MnSe (Figure S4) and MnSe@MWCNT (Figure 5d) catalysts showed no shift in peaks and no additional peaks after 30 h of OER confirming that there were no structural changes in the catalytic composite. The PXRD patterns in Figure S5, demonstrate that the crystallinity and phase purity of the MnSe@MWCNT phases remained unchanged after 12 h of OER in alkaline media. Similarly, a comparison of SEM images before and after OER activity revealed retention of similar morphology

Table 1: Comparison of electrocatalytic parameters for OER.

OER	MnSe	MnSe@MWCNT	RuO_2
Onset potential / V	1.49	1.47	1.57
η @ 10 mA cm^{-2} / mV	310	290	380
Tafel slope / mV dec^{-1}	61.43	54.76	114.91
ECSA / cm^2	10.48	19.3	-
RF	37.03	68.2	-

for hydrothermally synthesized MnSe and MnSe@MWCNT samples, as shown in Figure S6. Hence, from the results of PXRD, XPS, SEM and Raman spectra, it could be concluded that there was no degradation or bulk transformation of either MnSe or MnSe@MWCNT catalysts after prolonged OER under anodic potential.

However, it must be noted that in contrast to the bulk material, surface of these electrocatalysts can exhibit varied physical and chemical properties post-activity owing to presence of surface unsaturation and reactive intermediate adsorption. Because a surface atom is not surrounded by uniform layer of atoms on all sides, these changes can have a major impact on the material's top atomic layer. This can result in different bonding potential of the surface atoms which makes it more reactive than the bulk atoms. Hence it is important to characterize the surface of these catalyst composites to correctly understand evolution of active catalyst interface. Identification of the active surface composition, especially for the metal chalcogenides, has become overtly important with the growing emphasis on these highly efficient catalytic systems. However, there still has been no consensus on the actual surface composition, and researchers worldwide are still trying to get an answer by gathering evidence from various techniques. In this project, we have attempted to correctly identify composition of the reactive surface through detailed surface analysis and electrochemical measurements. Hence in addition to investigating bulk compositional stability, the change in surface composition of MnSe@MWCNT electrocatalysts after extended period OER studies was investigated by Surface Raman spectroscopy integrated with XPS. Specifically, the experiment was performed by making sure that data was acquired from the same surface region by aligning the XPS analysis position precisely with the Raman analysis position. Figure 6a demonstrates the working principle of surface Raman spectra acquisition for MnSe@MWCNT composite. The region of investigation was focused on the central part of the functional electrode which was the most active area for OER. Such surface specific analysis can be utilized to accurately study evolution of the interface following active intermediate adsorption and conversion, thereby leading to identification of true composition of the catalyst surface. The Raman spectrum of MnSe@MWCNT composite electrode after OER activity has been shown in Figure 6b. As can be seen from the Raman spectra, the characteristic D- and G- bands at 1342 and 1572 cm^{-1} respectively, corresponding to the MWCNT, were visible in both MnSe@MWCNT and pristine MWCNT surfaces. Additionally, absorptions around 2680–2730 cm^{-1} were observed in both samples, which are believed to be the first overtone of the D- mode, commonly known as the G′ or 2D band. G′ is the Raman double-resonance mode caused by disorders and/or defect in the MWCNT side walls typically illustrates degree of crystallinity in the nanotube walls. The I_D/I_G ratio, which describes the structural disorder of MWCNT or graphene, is proportional to D-and G-band intensities.[65] After chronoamperometry stability studies under anodic (OER) potential, the I_D/I_G ratio changed from 1.15 to 1.3, showing the possible formation of additional defects on CNT surface which can be caused by considerable influence of prolonged period of OER activity. The peak for Se–Se stretching mode in MnSe were observed at 254.44 cm^{-1}.[60,66] The sharp and broad peak at 636 cm^{-1} can be attributed to the Mn-Se stretching mode, which is consistent with earlier report.[61] After OER activity a small peak appeared at 738 cm^{-1} which can be ascribed to asymmetric stretching vibrations of SeO_2 groups. However, the major Raman peaks at the surface were still consistent with MnSe phase, suggesting that the composition and structure of the catalyst surface remained unchanged after chronoamperometry studies. It must be noted here that the surface Raman analysis after OER failed to pick up any evidence for the formation of a Mn-oxide or hydroxide layer on the surface confirming that the MnSe layer was indeed stable under continuous exposure at the low anodic potential required for OER. Interestingly, an additional Raman peak at 746 cm^{-1} was observed after OER (inset of Figure 6b) that could be assigned to formation of a local Mn=O cluster as has been proposed very recently,[67] wherein, the authors have identified evolution of active surface species through formation of this Mn-oxo linkage. In this article we propose that OER on MnSe surface occurs through formation of similar Mn-O linkages (as evidenced by the Raman peak at 746 cm^{-1}) on the selenide layer following the activation step initiated by -OH adsorption on the surface. This observation of formation of such (oxy)selenide as the active surface composition for MnSe-based catalyst composite further confirms our earlier observation that transition metal selenide catalysts evolve into mixed anionic (hydroxy)chalcogenide surface during OER.[8] Accurate elucidation of the active surface composition will be transformative for the field and will add critical knowledge for performing interface engineering and optimal catalyst surface design. Figure S7, shows the high resolution XPS spectra of Mn, Se and C after 12 h OER activity collected at the same spot of Raman spectral analysis. The XPS peaks before and after catalytic activity did not demonstrate any shift in Mn 2p and Se 3d peak locations. Both surface Raman and XPS indicating that there was no change in the surface composition of the MnSe@MWCNT.

Electrocatalytic Performance for ORR

Apart from the intriguing OER performance, the as-synthesized MnSe nanocomposite-based electrodes also exhibits efficient ORR electrocatalytic activity, as illustrated in Figure 7. The ORR activity was investigated through LSV measured in O_2-saturated 1 M KOH with rotating disk electrodes (RDE) set -up at scanning frequencies of 10 mV s^{-1} and rotation rates of 400, 800, 1200, 1600 and 2000 rpm.

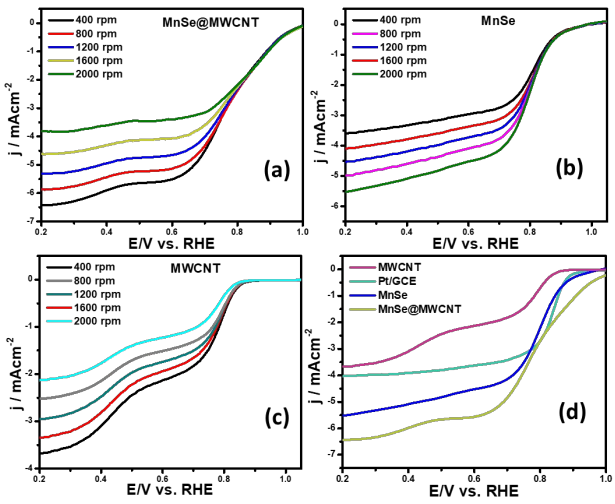

Figure 7. Linear sweep voltammograms of (a) MnSe@MWCNT (b) MnSe (c) MWCNT modified electrodes collected using RDE set-up. (d) Comparison of ORR activity of these catalysts at rotating speed of 2000 rpm.

LSV data for the MnSe@MWCNT, MnSe, MWCNT are shown in Figure 7 (a-d). The ORR activity of these Mn-based electrocatalysts were compared with electrodeposited Pt on GCE, which shows standard ORR activity as previously reported (Figure S8).[11] The ORR activity was also compared with standard 20% Pt/C composite which showed an onset potential of 0.90 V vs RHE (Figure S9) as has been reported earlier.[44] It can be inferred from the polarization curves shown in Figure 7, that the measured current density increased with increasing rotation speed due to enhanced diffusion of electrolyte on the electrode surface. The diffusion limiting current densities, onset potential, and half-wave potential has been determined for MnSe, MnSe@MWCNT, MWCNT and Pt/GCE from these plots. The onset potentials and half-wave potentials of MnSe@MWCNT were obtained as 0.94 V and 0.86 V vs RHE, respectively along a diffusion limit current density of 6.49 mA/cm^2 which was observed to be highest among all electrocatalysts reported in this study. A bar plot of the limiting current density for different catalysts is shown in Figure 8b. It shows that MnSe@MWCNT electrode shows a current density of 6.02 mA/cm^2 at potential of 0.4 V (vs RHE). However, MWCNT, Pt/GCE, and MnSe shows significantly lower current density

$$n = \frac{4I_D}{I_D + I_R/N} \quad \text{Eq-6}$$

$$\%H_2O_2 = \frac{200\, I_R/N}{I_D + I_R/N} \quad \text{Eq-7}$$

of 3.06, 3.92 and 5.1 mA/cm^2, respectively. The MnSe@MWCNT composite electrode's superior ORR activity compared to each of its constituents (i.e., MWCNT or MnSe) indicates a synergistic effect, most likely caused by the additional electron transfer pathways facilitated by the highly conductive MWCNT network.

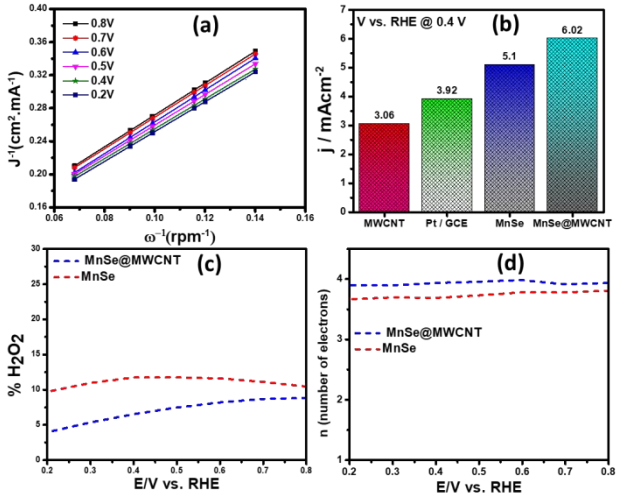

Figure 8. (a) K-L plots of MnSe@MWCNT composite electrode in O_2-saturated 1 M KOH. (b) Reduction current densities of MWCNT, Pt/GCE, MnSe, and MnSe@MWCNT. (c) H_2O_2 yield and (d) number of electrons for MnSe@MWCNT and MnSe modified electrodes at disc rotation speed of 1200 rpm and scan rate of 10 mV/s in O_2 saturated 1 M KOH.

These results demonstrate that it has much better activity than the precious metal based (Pt) catalyst for ORR electrocatalysis in an alkaline medium. To identify the role of a MWCNT as carbon support in the electrocatalytic behaviour of the composite, the electrocatalytic properties were of MWCNT also determined and compared to that of MnSe@MWCNT

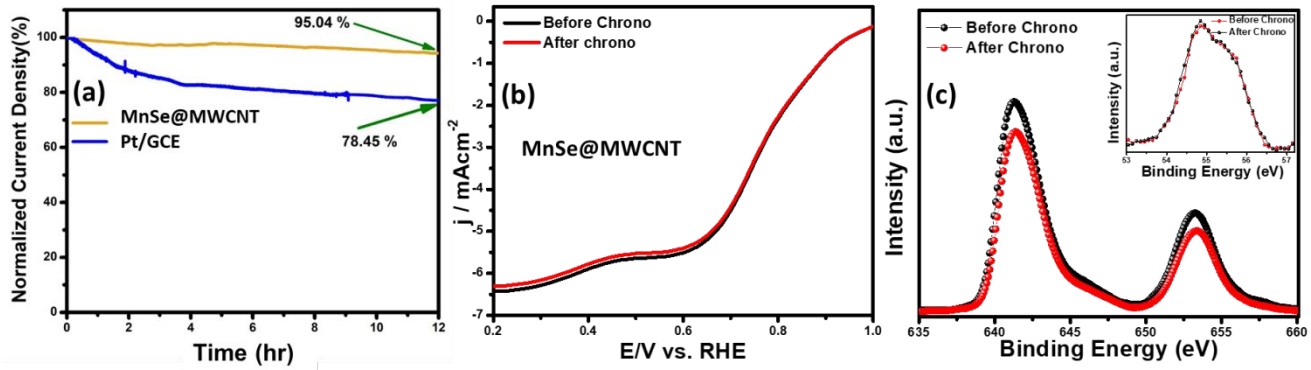

Figure 9. Durability test of MnSe@MWCNT and Pt/GCE composite electrodes in O_2-saturated 1 M KOH at a rotation speed of 1200 rpm. (b) LSV before and after chronoamperometry studies with MnSe@MWCNT. (c) Comparison of the XPS peaks of Mn 2p and Se 3d (Inset) before and after ORR chronoamperometry study.

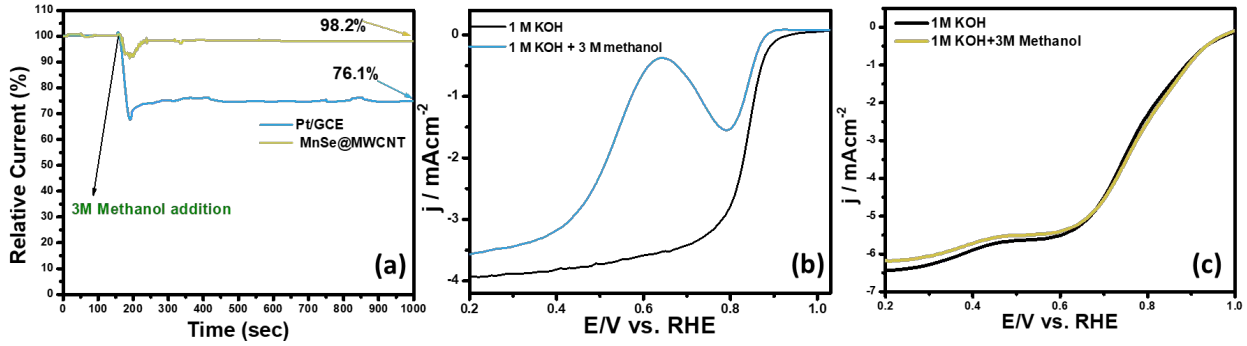

Figure 10. (a) Comparison of the methanol tolerance for MnSe@MWCNT and Pt/GCE composite electrode performed by adding methanol during chronoamperometry study. LSV plot for (b) Pt/GCE and (c) MnSe@MWCNT electrode in O_2-saturated 1 M KOH and 1 M KOH + 3 M methanol.

composite as shown in Figure 7 c and d. It was observed that while MWCNT was active for ORR, the MnSe@MWCNT composite had much superior activity both in terms of onset potentials and limiting current density. This can be explained from synergistic effect, wherein, MnSe on MWCNT surfaces provides active sites for electrocatalytic activity, while MWCNTs provide conducting channels for efficient charge transfer and a large surface area, resulting in highly active electrocatalyst for ORR.[44] To obtain a more thorough understanding of the ORR electrocatalytic activity of these catalysts, further electrochemical analyses were carried out. Koutecky-Levich (K-L) curves were plotted at different potentials, as shown in Figure 8a. The first-order reaction kinetics of dissolved oxygen with respect to dissolved oxygen concentration can be deduced from the linearity of the K-L graphs. The parallel behavior of the fitted lines also suggests similar electron transfer pathways for ORR at different potentials. The disk current (I_D) and the ring current (I_R) obtained with RRDE set-up was used to quantify the percentage of intermediate hydrogen peroxide, H_2O_2 production and the number of electrons (n) transferred**.** The H_2O_2 yield (%) and n were calculated using the following Eqs. (6) and (7), respectively.

The number of electrons transferred (n) for MnSe@MWCNT was estimated to be 3.96 at potential range of 0.8–0.2V, respectively, from the slope of Koutecky-Levich plots, indicating a dominant four-electron reduction pathway in 1 M KOH solution forming water as the reduction product. MnSe by itself showed a n value of 3.84 indicative of 4-electron pathway, while MWCNT showed n value of 2.86, indicating significant deviation form 4-electron reduction pathway. Further proof for this reaction path has been obtained from electrochemical analysis using the rotating ring-disk electrode (RRDE) set-up to identify and quantify the reduction product.

The general reduction of oxygen occurs with two consecutive two-electron transfer processes that lead to the formation of a peroxide species (HO_2^-) which will thereafter yield hydrogen peroxide. The final form of hydroxide (OH^-) is consequently reduced by two more electrons. Whereas the direct four-electron method directly reduces O_2 to OH. Consequently, RRDE is considered a reliable and commonly used technique for studying the ORR catalytic pathway by detecting the formation of HO_2^-. Figure 8c and 8d, show the electron transfer numbers and HO_2^- yields from RRDE data for MnSe and MnSe@MWCNT. The estimated H_2O_2 yield, as can be shown, is less than 10% and 12% for MnSe@MWCNT and MnSe respectively, over the potential range of 0.8–0.2 V vs RHE. These observations indicate that the ORR pathway catalysed by MnSe and MnSe@MWCNT is primarily a 4-electron mechanism through the direct formation of hydroxyl species and water as final products, similar to commercially available Pt/GCE catalysts. It was also observed that the rate of H_2O_2 production decreased remained constant for MnSe over the applied potential range, while it

Table 2. Comparison of electrocatalytic parameters for ORR.

Catalysts	ORR Performance Without Methanol addition				ORR Performance after Methanol addition		
	E_{onset} vs. RHE(V)	$E_{1/2}$	No. of transferred electrons	Diffusion Limited current density (mA cm^{-2})	E_{onset} vs. RHE(V)	$E_{1/2}$	Diffusion Limited current density (mA cm^{-2})
MnSe@ MWCNT	0.94	0.86	3.96	6.02	0.94	0.86	5.91
MnSe	0.91	0.82	3.84	5.1	-	-	-
MWCNT	0.83	0.79	2.86	3.06	-	-	-
Pt/GCE	0.92	0.81	3.94	3.92	0.87		3.61

decreased slightly for MnSe@MWCNT composite. The electron transfer rate in the MnSe@MWCNT composite can be expected to be higher than MnSe based film due to presence of MWCNT network which facilitates charge transfer. Hence, at more cathodic potentials, as rate of O_2 reduction reaches maximum, it leads to faster conversion to H_2O through 4 electron reduction pathways compared to that of H_2O_2 (2e reduction) on the MnSe@MWCNT composite film. This faster conversion to H_2O can be supported on MnSe@MWCNT composite film due to its highly conducting nature, while for MnSe film, limited conductivity leads to steady conversion rate for H_2O and H_2O_2. Hence there is a decrease in H_2O_2 yield for MnSe@MWCNT at more cathodic potential.

The durability and stability of the catalysts are also essential to their functional applications, in addition to the superior catalytic performance. In Figure 9a, the long-term stability of the composite catalyst MnSe@MWCNT and Pt/GCE for ORR was checked through constant potential chronoamperometry study at $E_{1/2}$ potential and comparing the LSV plots in O_2-saturated 1 M KOH before and after 12 h of chronoamperometry studies. The LSV plot of the MnSe@MWCNT catalyst has been shown in Figure 9b, at rotational speeds of 2000 rpm before and after chronoamperometry. It can be seen that after the stability test, $E_{1/2}$ remains at the same potential. In comparison, following similar testing, the $E_{1/2}$ of Pt/GCE catalyst moves to lower potential by more than ~20 mV (Figure S10), suggesting the superior stability of the MnSe@MWCNT composite electrode for ORR activity compared to Pt/GCE. The robust connection between MnSe nanoparticles and MWCNT network, which maintains structural integrity for efficient charge transfer, could be responsible for MnSe@MWCNT's superior stability for ORR activity as well. Table 2 represents the comparison of electrocatalytic parameters of all the catalysts for ORR activity reported in this article.

The compositional stability of the composite electrode after prolonged ORR activity was confirmed through XPS. The XPS spectra of MnSe@MWCNT before and after ORR stability test as shown in Figure 9c, confirmed that the composition of the catalyst was retained. XPS spectra obtained from the MnSe@MWCNT composite after prolonged ORR was superimposable with the as-prepared composite as shown in Figure 9c, indicating no catalyst degradation.

The methanol crossover effect and functional durability are some of the key criteria for assessment of cathode stability in direct methanol fuel cells. In Figure 10a, the catalyst-coated electrode's methanol crossover effect was determined by measuring the chronoamperometric response in O_2-saturated 0.1 M KOH following the addition of 3 M methanol. RDE LSV plots of MnSe@MWCNT and the Pt/GCE in O_2-saturated 3 M CH_3OH + 1 M KOH solution are shown in Figure 10b and 10c. In the presence of methanol, ORR on Pt/GCE overlapped with methanol oxidation because Pt is active in the ORR potential zone for methanol oxidation leading to the reduction in ORR activities. However, the polarization curves for MnSe@MWCNT composite electrode in the presence of methanol showed no loss of activity as can be seen in Figure 10c, indicating high degree of methanol tolerance. In contrast, a methanol oxidation peak for the Pt/GCE electrode appears at 0.59 V. Pt/GCE also exhibited a current loss of 24 % following the addition of methanol after 1000 seconds as illustrated in the chronoamperometric response (Figure 10a), while the current remained very stable for MnSe@MWCNT catalyst composite, indicating that this electrode is highly selective to ORR even in the presence of copious quantities of methanol. The i–t curve in Figure 10a, clearly demonstrates the excellent retention of the current density of around 98.2% for MnSe@MWCNT catalyst in presence of methanol, asserting its commercial viability in direct methanol fuel cells.

As discussed in the preceding sections, the synergistic effects between MnSe and MWCNT may explain the MnSe/MWCNT composite's remarkable methanol tolerance performance. Since each material (MnSe or MWCNT) alone has only moderate ORR and OER activity, the synergistic integration of MnSe and MWCNT provides excellent bifunctional electrocatalytic efficiency. Furthermore, MnSe particles dispersed within MWCNT networks not only provide the most active sites for catalysis, but can also effectively restrain catalyst particle aggregation, detachment, and Ostwald ripening, boosting electrocatalytic stability. The onset potential along with other electrocatalytic parameters of MnSe@MWCNT is comparable with some of the best-known ORR electrocatalysts reported till date as shown in Table S3, (Supporting Information).

To get a better insight into the possible synergistic effect between catalyst and carbon nanostructures, the electrochemical impedance spectroscopy (EIS) of MnSe and MnSe@MWCNT catalysts was measured within a frequency range of 10^5–0.01 Hz is shown in Fig. 11. The inset of Fig. 11 shows a simple equivalent circuit model that was used to fit the EIS data wherein R_f represents the resistance of the catalyst composite, R_{CT} the charge transfer resistance at the electrode-electrolyte interface, Z_W the Warburg impedance, and CPE the

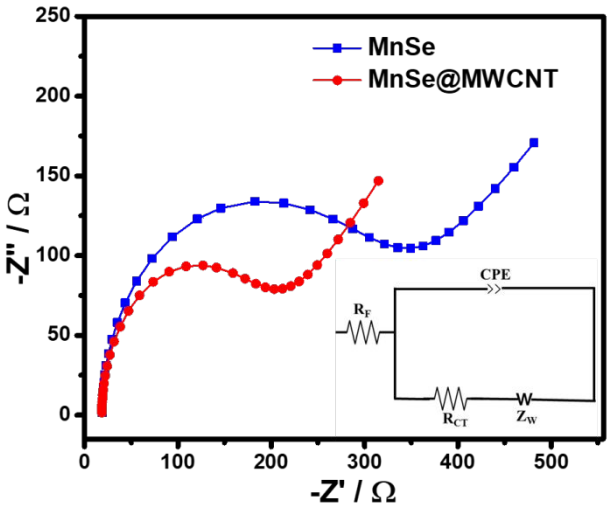

Figure 11. Nyquist plots of MnSe and MnSe@MWCNT composite electrodes in AC frequency range between 100 kHz and 0.1 Hz. Inset shows the fitted equivalent circuit.

constant phase element. All these circuit elements were estimated from fitting of the equivalent circuit to the impedance plot and represented in Table S4. As shown at Figure 11, the charge transfer resistance of the MnSe@MWCNT (R_{CT}) was estimated to be 18.6 Ω and the value is substantially lower than that of MnSe (28.4 Ω). The resistance of the MnSe@MWCNT composite film was also lower than that of MnSe indicating better charge transfer within the catalyst composite. This observation further confirmed that addition of MWCNT is beneficial for increasing charge transfer within the catalyst composite and electrode-electrolyte interface resulting in enhancement of electrocatalytic performance for MnSe@MWCNT composite electrode.

Conclusions

In summary, we have synthesized a manganese selenide based highly efficient bifunctional electrocatalyst active for OER and ORR in alkaline medium. Simple one-pot hydrothermal synthesis yielded these nanostructured catalysts. OER activity of MnSe could be further improved by forming a composite with MWCNT, whereby the MnSe@MWCNT modified electrode shows a very low overpotential of 290 mV at 10 mA cm^{-2}. Apart from low overpotential, MnSe and MnSe@MWCNT modified electrodes also exhibit exceptional functional and compositional stability after prolonged exposure in alkaline medium under anodic potential. Detailed surface analysis revealed formation of oxychalcogenide as the active surface species explaining its high activity and stability. Furthermore, this composite electrode was also tested for methanol tolerance during ORR. The MnSe@MWCNT electrode shows excellent methanol tolerance surpassing the state-of-the-art Pt/C electrocatalyst. Nanostructured MnSe on MWCNT surfaces provides active sites for electrocatalytic activity, while the MWCNT provides conducting channels and a large surface area. Hence, the high efficiency of electrocatalytic activity for MnSe@MWCNT electrode can be attributed primarily to facile charge transfer within the catalyst composite and at the catalyst-electrode interface, its large surface area, abundance of active sites, and higher degree of surface roughness. The development of non-precious metal based nanostructured electrocatalyst composites will be expedited by this work leading to advancement in renewable energy conversion and storage.

Conflicts of interest

There are no conflicts to declare.

Acknowledgements

The authors would like to acknowledge financial support from NAF (DMR 1710313) and Materials Research Centre (MRC), Missouri S&T for equipment usage.

Notes and references

1 L. Shi, T. Zhao, A. Xu and Z. Wei, *ACS Catal.*, 2016, **6**, 6285–6293.

2 J. Greeley, I. E. L. Stephens, A. S. Bondarenko, T. P. Johansson, H. A. Hansen, T. F. Jaramillo, J. Rossmeisl, I. Chorkendorff and J. K. Nørskov, *Nat. Chem. 2009 17*, 2009, **1**, 552–556.

3 Wei Yang, Wenbin Gong, Yanhong Shi, Xiaona Wang, Yulian Wang, Jian Qiao, Sha Zeng, Jiangtao Di and Qingwen Li, *J. Mater. Chem. A*, , DOI:10.1039/D1TA03048E.

4 Y. F. Xu, Y. Chen, G. L. Xu, X. R. Zhang, Z. Chen, J. T. Li, L. Huang, K. Amine and S. G. Sun, *Nano Energy*, 2016, **28**, 63–70.

5 H. Radinger, P. Connor, R. Stark, W. Jaegermann and B. Kaiser, *ChemCatChem*, 2021, **13**, 1175–1185.

6 S. Umapathi, J. Masud, A. T. Swesi and M. Nath, *Adv. Sustain. Syst.*, 2017, **1**, 1–11.

7 A. T. Swesi, J. Masud and M. Nath, *Energy Environ. Sci.*, 2016, **9**, 1771–1782.

8 U. De Silva, J. See, W. P. R. Liyanage, J. Masud, J. Wu, W. Yang, W.-T. Chen, D. Prendergast and M. Nath, *Energy & Fuels*, 2021, **35**, 4403.

9 O. Mabayoje, A. Shoola, B. R. Wygant and C. B. Mullins, *ACS Energy Lett.*, 2016, **1**, 195–201.

10 Y. Lyu, J. Zheng, Z. Xiao, S. Zhao, S. P. Jiang and S. Wang, *Small*, 2020, **16**, 1906867.

11 J. Masud and M. Nath, *ACS Energy Lett.*, 2016, **1**, 27–31.

12 Y. Cheng, S. He, S. Lu, J. Veder, B. Johannessen, L. Thomsen, M. Saunders, T. Becker, R. De Marco, Q. Li, S. Yang and S. P. Jiang, *Adv. Sci.*, 2019, **6**, 1802066.

13 S. Guo, S. Zhang, L. Wu and S. Sun, *Angew. Chemie Int. Ed.*, 2012, **51**, 11770–11773.

14 J. Masa, W. Xia, I. Sinev, A. Zhao, Z. Sun, S. Grützke, P. Weide, M. Muhler and W. Schuhmann, *Angew. Chemie Int. Ed.*, 2014, **53**, 8508–8512.

15 M. Nath, U. De Silva, H. Singh, M. Perkins, W. P. R. Liyanage, S. Umapathi, S. Chakravarty and J. Masud, *ACS Appl. Energy Mater.*, 2021, acsaem.1c01438.

16 B. S. Lee, H. Y. Park, M. K. Cho, J. W. Jung, H. J. Kim, D. Henkensmeier, S. J. Yoo, J. Y. Kim, S. Park, K. Y. Lee and J. H. Jang, *Electrochem. commun.*, 2016, **64**, 14–17.

17 F. D. Kong, S. Zhang, G. P. Yin, N. Zhang, Z. B. Wang and C. Y. Du, *Electrochem. commun.*, 2012, **14**, 63–66.

18 D. Mladenović, D. M. F. Santos, G. Bozkurt, G. S. P. Soylu, A. B. Yurtcan, Š. Miljanić and B. Šljukić, *Electrochem. commun.*, 2021, **124**, 106963.

19 M. Shamsuddin Ahmed, B. Choi and Y.-B. Kim, *Sci. REpORTS |*, 2018, **8**, 2543.

20 J. Masa, W. Xia, I. Sinev, A. Zhao, Z. Sun, S. Grützke, P. Weide, M. Muhler and W. Schuhmann, *Angew. Chemie*, 2014, **126**, 8648–8652.

21 Y. Hao, Y. Xu, J. Liu and X. Sun, *J. Mater. Chem. A*, 2017, **5**, 5594–5600.

22 C. F. Chen, G. King, R. M. Dickerson, P. A. Papin, S. Gupta, W. R. Kellogg and G. Wu, *Nano Energy*, 2015, **13**, 423–432.

23 X. Cao, E. Johnson and M. Nath, *J. Mater. Chem. A*, 2019, **7**, 9877–9889.

24 W. Zhong, B. Xiao, Z. Lin, Z. Wang, L. Huang, S. Shen, Q. Zhang and L. Gu, *Adv. Mater.*, 2021, **33**, 2007894.

25 M. Sun, R.-T. Gao, X. Liu, R. Gao and L. Wang, *J. Mater. Chem. A*, 2020, **8**, 25298–25305.
26 G. Mei, H. Liang, B. Wei, H. Shi, F. Ming, X. Xu and Z. Wang, *Electrochim. Acta*, 2018, **290**, 82–89.
27 S. Umapathi, H. Singh, J. Masud and M. Nath, *Mater. Adv.*, , DOI:10.1039/D0MA00890G.
28 H. Singh, J. Bernabe, J. Chern and M. Nath, *J. Mater. Res.*, 2021, **36**, 1413–1424.
29 M. Z. Xue and Z. W. Fu, *Electrochem. commun.*, 2006, **8**, 1855–1862.
30 B. G. Amin, J. Masud and M. Nath, *RSC Adv.*, 2019, **9**, 37939–37946.
31 P. D. Matthews, P. D. McNaughter, D. J. Lewis and P. O'Brien, *Chem. Sci.*, 2017, 8, 4177–4187.
32 J. He, A. Bhargav, H. Yaghoobnejad Asl, Y. Chen and A. Manthiram, *Adv. Energy Mater.*, 2020, **10**, 2001017.
33 A. Saxena, W. Liyanage, J. Masud, S. Kapila and M. Nath, *J. Mater. Chem. A*, 2021, **6**, 4883–5230.
34 J. Masud, P.-C. Ioannou, N. Levesanos, P. Kyritsis and M. Nath, *ChemSusChem*, 2016, **9**, 3128–3132.
35 F. Cheng, Y. Su, J. Liang, Z. Tao and J. Chen, *Chem. Mater.*, 2009, **22**, 898–905.
36 S. Sun, H. Miao, Y. Xue, Q. Wang, S. Li and Z. Liu, *Electrochim. Acta*, 2016, **214**, 49–55.
37 Y. Zhong, X. H. Xia, F. Shi, J. Y. Zhan, J. P. Tu and H. J. Fan, *Adv. Sci.*, , DOI:10.1002/advs.201500286.
38 D. Chao, J. Wang, C. Zhu, D. Gao and ab Jun Ding, *This J. is Cite this Chem. Soc. Rev*, **47**, 4332.
39 P. P. Patel, M. K. Datta, O. I. Velikokhatnyi, R. Kuruba, K. Damodaran, P. Jampani, B. Gattu, P. M. Shanthi, S. S. Damle and P. N. Kumta, *Sci. Rep.*, 2016, **6**, 1–14.
40 N. Kazimova, K. Ping, M. Alam, M. Danilson, M. Merisalu, J. Aruväli, P. Paiste, M. Käärik, V. Mikli, J. Leis, K. Tammeveski, P. Starkov and N. Kongi, *J. Catal.*, 2021, **395**, 178–187.
41 D. M. Morales, M. A. Kazakova, S. Dieckhöfer, A. G. Selyutin, G. V. Golubtsov, W. Schuhmann and J. Masa, *Adv. Funct. Mater.*, 2020, **30**, 1905992.
42 S. H. Yetgin, *J. Mater. Res. Technol.*, 2019, **8**, 4725–4735.
43 M. N. Norizan, M. H. Moklis, S. Z. Ngah Demon, N. A. Halim, A. Samsuri, I. S. Mohamad, V. F. Knight and N. Abdullah, *RSC Adv.*, 2020, **10**, 43704–43732.
44 M. S. Ahmed, B. Choi and Y.-B. Kim, *Sci. Rep.*, 2018, **8**, 2543.
45 O. A. Oyetade and R. J. Kriek, *Electrocatal. 2019 111*, 2019, **11**, 35–45.
46 D. M. Morales, M. A. Kazakova, S. Dieckhöfer, A. G. Selyutin, G. V. Golubtsov, W. Schuhmann and J. Masa, *Adv. Funct. Mater.*, 2020, **30**, 1905992.
47 Y.-L. Zhang, K. Goh, L. Zhao, X.-L. Sui, X.-F. Gong, J.-J. Cai, Q.-Y. Zhou, H.-D. Zhang, L. Li, F.-R. Kong, D.-M. Gu and Z.-B. Wang, *Nanoscale*, 2020, **12**, 21534–21559.
48 M. Tavakkoli, E. Flahaut, P. Peljo, J. Sainio, F. Davodi, E. V. Lobiak, K. Mustonen and E. I. Kauppinen, *ACS Catal.*, 2020, **10**, 4647–4658.
49 D. M. Morales, M. A. Kazakova, S. Dieckhöfer, A. G. Selyutin, G. V. Golubtsov, W. Schuhmann and J. Masa, *Adv. Funct. Mater.*, 2020, **30**, 1905992.
50 A. P. Tiwari, D. Kim, Y. Kim and H. Lee, *Adv. Energy Mater.*, 2017, **7**, 1602217.
51 M. Sakthivel and J. F. Drillet, *Appl. Catal. B Environ.*, 2018, **231**, 62–72.
52 H. Singh, S. Zhuang, B. Ingis, B. B. Nunna and E. S. Lee, *Carbon N. Y.*, 2019, 151, 160–174.
53 Y. Min, G. D. Moon, C. E. Kim, J. H. Lee, H. Yang, A. Soon and U. Jeong, *J. Mater. Chem. C*, 2014, 2, 6222–6248.
54 S. Mishra, K. Song, K. C. Ghosh and M. Nath, *ACS Nano*, 2014, **8**, 2077–2086.
55 Jianwei Su, Guoliang Xia, Ran Li, Yang Yang, Jitang Chen, Ruohong Shi, Peng Jiang and Qianwang Chen, *J. Mater. Chem. A*, 2016, **4**, 9204–9212.
56 Suho Jung, C. C. L. McCrory, I. M. Ferrer, J. C. Peters and T. F. Jaramillo, *J. Mater. Chem. A*, 2016, **4**, 3068–3076.
57 G. K. H. Wiberg, K. J. J. Mayrhofer and M. Arenz, *Fuel Cells*, 2010, **10**, 575–581.
58 Q. Zhao, D. Zhong, L. Liu, D. Li, G. Hao and J. Li, *J. Mater. Chem. A*, 2017, **5**, 14639–14645.
59 A. T. Swesi, J. Masud and M. Nath, *J. Mater. Res.*, 2016, **31**, 2888–2896.
60 A. Milutinovi, Z. V Popovi, N. Tomi and S. Devi, *Raman Spectroscopy of Polycrystalline-MnSe*, 2004.
61 S. Sahoo, P. Pazhamalai, K. Krishnamoorthy and S. J. Kim, *Electrochim. Acta*, 2018, **268**, 403–410.
62 L. Thi Mai Hoa, *Diam. Relat. Mater.*, 2018, **89**, 43–51.
63 H. Tang, X. Lu, H. Zhu, Y. Tian, R. Khatoon, Z. Zhu, Y.-J. Zeng, Q. Zhang and J. Lu, , DOI:10.1007/s11581-019-03180-5.
64 S. Rana, K. K. Yadav, S. K. Guchhait, S. T. Nishanthi, S. K. Mehta and M. Jha, *J. Mater. Sci.*, 2021, **56**, 8383–8395.
65 L. G. Cançado, A. Jorio, E. H. M. Ferreira, F. Stavale, C. A. Achete, R. B. Capaz, M. V. O. Moutinho, A. Lombardo, T. S. Kulmala and A. C. Ferrari, *Nano Lett.*, 2011, **11**, 3190–3196.
66 J. Kucharek, R. Bożek and W. Pacuski, *Jaszowiec*, , DOI:10.12693/APhysPolA.136.598.
67 K. H. Cho, S. Park, H. Seo, S. Choi, M. Y. Lee, C. Ko and K. T. Nam, *Angew. Chemie*, 2021, **133**, 4723–4731.